

Full paper



Sputter-deposited TiO_x thin film as a buried interface modification layer for efficient and stable perovskite solar cells

Xiongzhuo Jiang^a, Jie Zeng^b, Kun Sun^a, Zerui Li^a, Zhuijun Xu^a, Guangjiu Pan^a, Renjun Guo^{c,d}, Suzhe Liang^a, Yusuf Bulut^{a,e}, Benedikt Sochor^e, Matthias Schwartzkopf^e, Kristian A. Reck^f, Thomas Strunskus^f, Franz Faupel^f, Stephan V. Roth^{e,g}, Baomin Xu^{b,*}, Peter Müller-Buschbaum^{a,*}

^a Technical University of Munich, TUM School of Natural Sciences, Department of Physics, Chair for Functional Materials, James-Frank-Str. 1, Garching 85748, Germany

^b Department of Materials Science and Engineering, Southern University of Science and Technology, Shenzhen 518055, China

^c Karlsruhe Institute of Technology, Hermann-von-Helmholtz-Platz 1, Eggenstein-Leopoldshafen 76344, Germany

^d Solar Energy Research Institution of Singapore, National University of Singapore, 7 Engineering Drive 1, #06-01 Block E3A, 117574, Singapore

^e Deutsches Elektronen-Synchrotron DESY, Notkestrasse 85, Hamburg 22607, Germany

^f Chair for Multicomponent Materials, Department of Materials Science, Kiel University, Kaiserstr. 2, Kiel 24143, Germany

^g KTH Royal Institute of Technology, Department of Fibre and Polymer Technology, Teknikringen 56-58, Stockholm SE-100 44, Sweden

ARTICLE INFO

Keywords:

Perovskite solar cells
Sputter deposition
Buried interface layer
Titania
In situ study

ABSTRACT

Despite perovskite solar cells (PSCs) based on a SnO₂ hole-blocking layer (HBL) are achieving excellent performance, the non-perfect buried interface between the SnO₂ HBL and the perovskite layer is still an obstacle in achieving further improvement in power conversion efficiency (PCE) and stability. The poor morphology with numerous defects and the energy level mismatch at the buried interface constrain the open circuit voltage and cause instability. Herein, a sputter-deposited TiO_x thin film is used as a buried interface modification layer to address the aforementioned issues. Utilizing *in situ* grazing-incidence small-angle X-ray scattering (GISAXS) during the sputter deposition, we monitor and unveil the growth process of the TiO_x thin film, identifying a 10 nm thickness optimum. The defects at the buried interface are passivated through tuning the growth, leading to a suppressed non-radiative recombination and improved PCE (from 22.19 % to 23.93 %). The evolution of the device performance and the degradation process of PSCs using *operando* grazing-incidence wide-angle X-ray scattering (GIWAXS) under the protocol ISOS-L-II explains the enhanced stability introduced by the buried interface modification via a sputter-deposited TiO_x thin layer. The perovskite decomposition process and the detrimental formation of PbI₂ are both slowed down by the TiO_x thin layer.

1. Introduction

Halide perovskite material is regarded as an excellent light absorber for solar cells because of its remarkable characteristics, such as high absorption coefficient, long charge carrier lifetime, and tunable bandgap for maximizing the absorption of the solar spectrum [1,2]. With these remarkable properties, perovskite solar cells (PSCs) can achieve a competitive power conversion efficiency (PCE). Over the past decade, PSCs have received tremendous attention due to their ever-increasing PCE, from an initial value of 3.8 % to an excellent certificated value of 26 %, close to the level of silicon solar cells [3,4]. Nevertheless, the PCE

of the start-of-art devices is still below its maximum theoretical PCE (>30 %) according to the Shockley–Queisser (S–Q) limit, indicating that there is ample space for PCE improvement [5]. In view of the complicated multi-layer structure of PSCs, there are numerous reports about the improvement of their performance, including composition optimization of perovskite crystal [6], exploration of anti-solvent systems [7], improvement in hole and electron blocking layers [8], and the modification of the perovskite surface and buried interfaces [9]. Among them, the buried interface modification has been spotlighted recently because of its high potential to improve the PCE alongside with the stability of PSCs [10].

* Corresponding authors.

E-mail addresses: subm@sustech.edu.cn (B. Xu), muellerb@ph.tum.de (P. Müller-Buschbaum).

<https://doi.org/10.1016/j.nanoen.2024.110360>

Received 26 July 2024; Received in revised form 9 October 2024; Accepted 10 October 2024

Available online 11 October 2024

2211-2855/© 2024 The Author(s). Published by Elsevier Ltd. This is an open access article under the CC BY license (<http://creativecommons.org/licenses/by/4.0/>).

Traditionally, the compact TiO₂/mesoporous TiO₂ stack or compact TiO₂-only layer is a critical component in regular PSCs, owing to its good energy level match with the perovskite [11]. However, a high processing temperature (~ 500°C) is required to reach the desired crystallinity of TiO₂, which consumes more energy and limits its commercial application [12]. Compared with TiO₂, SnO₂ allows for a lower fabrication temperature and, meanwhile, is more commonly used because of an easier fabrication as well as better optical and electrical properties [13]. However, although SnO₂-based PSCs exhibit superior efficiency and stability, the non-perfect buried interface between the SnO₂ hole-blocking layer (HBL) and the perovskite layer is still an obstacle to further improvement of the device performance [14]. According to previous reports, the defect density at the buried interface is much higher than in the bulk of the perovskite layer [15]. Therefore, the non-radiative recombination at the buried interface caused by these defects is a critical factor for the open voltage V_{OC} losses, which constrain the PCE of PSCs [16]. In addition, defects play an important role in inducing perovskite degradation [17]. Solution-processed SnO₂, especially those fabricated with the spin coating method, show a poor morphology due to the colloidal particle agglomeration driven by van der Waals interaction forces, which brings the possibility of non-fully covered indium tin oxide (ITO) or fluorine-doped tin oxide (FTO) substrates [18].

To address the poor morphology of the SnO₂ HBL and reduce the defect density, a large number of researchers constructed a composite HBL mixed with SnO₂ and TiO₂, including the TiO₂/SnO₂ bilayer and the TiO₂/SnO₂ mixed layer [19]. For the bilayer approach of the HBL, the TiO₂ has to be put at the bottom side (contact with substrate), while the SnO₂ is constructed on the upper side (contact with perovskite). This sequence is caused by the different fabrication conditions of both layers: A high fabrication temperature (about 500°C) is required for TiO₂, but a much lower temperature (about 150°C) is needed for SnO₂ [20]. Such bilayer TiO₂/SnO₂ HBL showed enhanced film quality with a fully covered surface, thus resulting in a better contact interface with the perovskite layer [21]. To improve the adhesion between the inorganic HBL and a polymer substrate in flexible PSCs, TiO₂ nanosol as an inorganic binder was mixed with SnO₂ colloidal nanoparticles to obtain a TiO₂-SnO₂ hybrid HBL [22]. Based on this hybrid HBL, PSCs were realized with a PCE of 21.02 %. These reports indeed achieve an improvement in the device performance. However, the TiO₂/SnO₂ bilayer does not have a perfect energy band arrangement due to the conduction band of TiO₂ being higher than SnO₂ in general, which is not good for the charge transport cascade [21,23,24]. In comparison, the SnO₂/TiO₂ bilayer shows a cascade energy band arrangement, which enables the electron extraction and transport from the perovskite layer smoothly [25,26]. Despite the SnO₂-TiO₂ hybrid exhibiting better mechanical reliability against bending due to the strong adhesion to the substrate compared with the SnO₂ colloid alone, the coverage issue remains due to the non-conformal growth induced by spin coating deposition. Therefore, a SnO₂/TiO₂ bilayer with a cascade energy band arrangement and a full coverage of the substrate should be developed for PSCs. However, a reversed bilayer structure having a TiO_x top- and SnO₂ bottom-layer is rarely reported. To the best of our knowledge, so far there is no report about an HBL combining a sputter-deposited TiO_x layer atop a SnO₂ layer for the use in PSCs, and the TiO_x thin film growth mechanism during sputter deposition is not clarified.

In the present work, we sputter deposited a TiO_x thin film on top of a SnO₂ HBL as a buried interface modification layer to improve the film morphology and reduce the defect concentration at the buried interface between perovskite and SnO₂. The structure evolution of the forming TiO_x thin film is unveiled in detail with the use of synchrotron radiation-based *in situ* grazing-incidence small-angle X-ray scattering (GISAXS). For comparison, sputter deposition TiO_x on bare ITO is studied as well. Optical and electric characterizations combined with a thorough understanding of the growth process point to a TiO_x thickness of 10 nm as optimum for the buried interface modification layer. For the related

PSCs, we observe that the non-radiative recombination is significantly suppressed due to the decreased defect density at the buried interface, improving the PCE from 22.19 % to 23.93 %. Furthermore, we investigate the operating stability of such PSCs under a nitrogen atmosphere using synchrotron radiation-based *operando* grazing-incidence wide-angle X-ray scattering (GIWAXS). The results show that the devices exhibit an enhanced stability after introducing the buried interface modification layer by the sputter-deposited TiO_x thin film due to a slowing down of the perovskite degradation. The formation of detrimental lead iodide (PbI₂) is reduced by the buried interface modification layer.

2. Results and discussion

2.1. TiO_x thin film growth during sputter deposition

There are numerous studies regarding the sputter deposition of TiO₂ as an HBL, but most of them focus on the effect of sputter-deposited TiO₂ on the device performance. For a deeper understanding, the nucleation and growth process of the TiO₂ thin film needs to be studied [27]. Understanding the TiO_x thin film growth is important for further optimization of sputter-deposited HBLs to achieve efficient and stable PSCs [28]. Thus, we observe the TiO_x thin film growth with *in situ* GISAXS during sputter deposition. To investigate the effects of different substrates on the TiO_x thin film growth, we sputter deposit TiO_x on top of two substrates: 1) pure ITO (denoted as ITO-TiO_x) and 2) ITO covered with spin-coated SnO₂ nanoparticles (denoted as SnO₂-TiO_x). Comparing the selected 2D GISAXS data of ITO-TiO_x and SnO₂-TiO_x samples (Figs. 1a-1d), after the sputter deposition, some faint intensity signals can be seen in the high q -value region ($q > 1.0 \text{ nm}^{-1}$) from the horizontal direction for ITO-TiO_x sample. Such signal originates from small structures being formed at the surface of ITO. In the vertical direction of 2D GISAXS data, pronounced intensity fringes and a Yoneda peak splitting are observed for both samples (Figs. 1b and 1d), indicating the successful sputter deposition of the TiO_x layer atop of both substrates. It is noted that there are already signals at the high q -value region in the horizontal direction before the start of sputter deposition for the SnO₂-TiO_x sample, which can be attributed to the X-ray scattering from the SnO₂ nanoparticles. An absence of X-ray beam damage is confirmed with scans after sputter deposition (Fig. S1).

The line cut mapping is an excellent way to survey the whole sputter deposition process of forming the TiO_x thin film. The contour plots extracted from vertical line cuts (an integrated q_y region at $q_y = 0.1 \text{ nm}^{-1}$ with $\Delta q_y = 0.034 \text{ nm}^{-1}$) of 2D GISAXS data for ITO-TiO_x and SnO₂-TiO_x samples are shown in Figs. 1e-1f. For both samples, the intensity maxima continuously shift to lower q -values, indicating a continuous increase in the effective thickness (δ_{TiO_x}) of the sputter-deposited TiO_x layer. With an increase in the thickness, a new Yoneda peak (TiO_x layer) appears due to the deposition of TiO_x, which density is different from the ITO substrate and SnO₂ layer densities (Fig. S2). In the contour plot extracted from the horizontal line cuts with an integrated q_z region of 0.6–0.7 nm^{-1} (Figs. 1g-1h), for the ITO-TiO_x sample, the signals at the high q -value region (above 1.0 nm^{-1}) are invisible before the effective thickness reaches 5 nm. This is regarded as the stage of nucleation. In contrast, for the SnO₂/TiO_x sample, the signals from the SnO₂ nanoparticles are mixed with TiO_x microstructure, resulting in the invisible signal change at the high q region. The final effective thickness of the TiO_x layer for ITO-TiO_x and SnO₂-TiO_x samples is 30.4 nm and 30.9 nm, respectively, as calculated from the vertical line cut data (Fig. S2). The final thickness of the TiO_x layer is further verified by the SEM cross-section images (Fig. S3).

To further investigate the TiO_x structure evolution, we fit the horizontal line cut data with a model based on the distorted wave-born approximation (DWBA). Figs. 2a-2b displays selected horizontal line cut data at different effective thicknesses of ITO-TiO_x and SnO₂-TiO_x samples, respectively. For both substrates, two characteristic structure

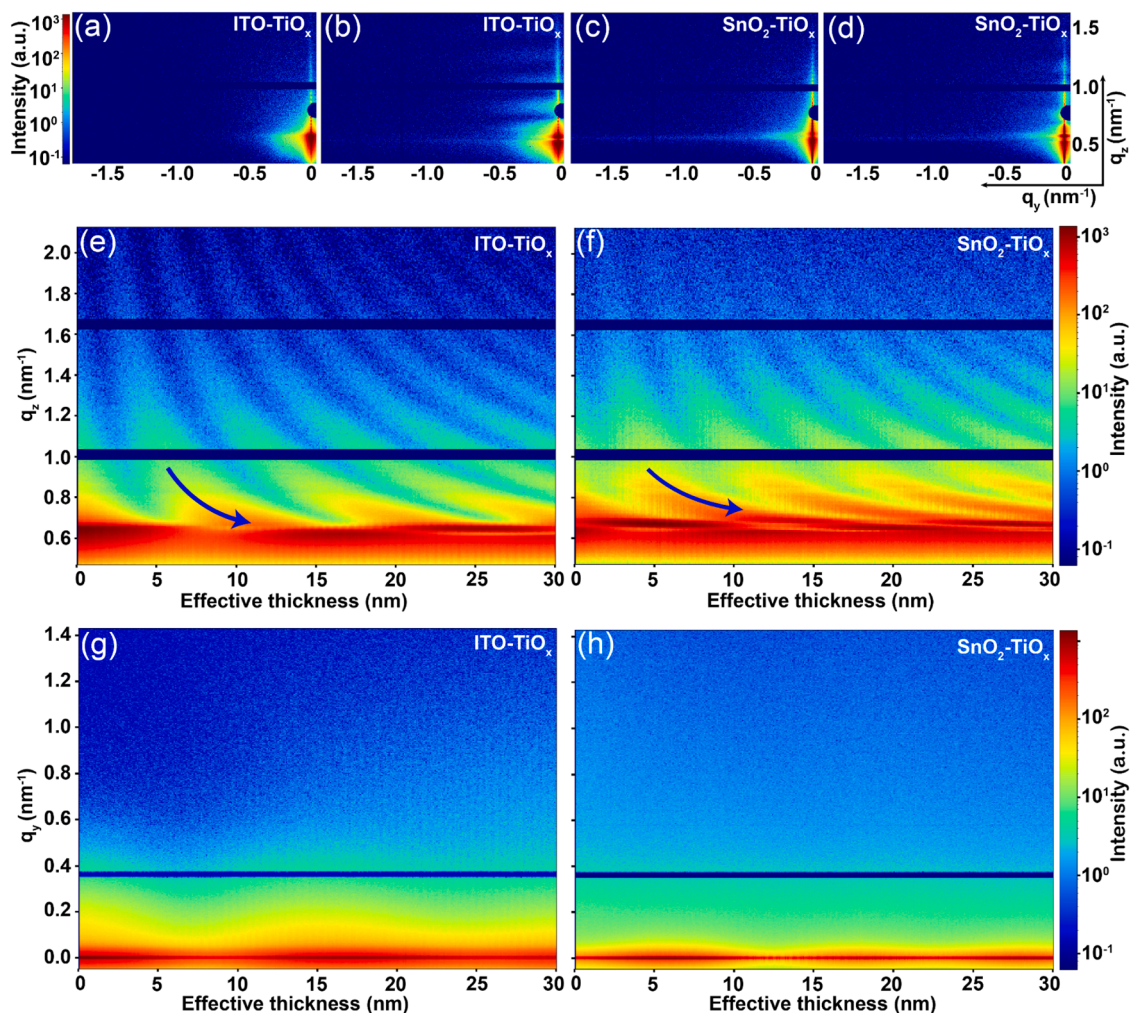


Fig. 1. Selected 2D GISAXS data: a) before and b) after sputter deposition of 30 nm TiO_x on top of pure ITO substrate, and c) before and d) after sputter deposition of 30 nm TiO_x on top of SnO_2 nanoparticle layer on ITO. Overview of the sputter deposited TiO_x thin film growth process: Contour plots as a function of the effective TiO_x thickness for the e) pure ITO substrate and f) SnO_2 nanoparticle layer onto ITO extracted from vertical line cuts at $q_y = 0.1 \text{ nm}^{-1}$ with $\Delta q_y = 0.034 \text{ nm}^{-1}$, and for the g) pure ITO substrate and h) SnO_2 nanoparticle layer onto of ITO extracted from horizontal line cuts with an integrated q_z region of $0.6\text{--}0.7 \text{ nm}^{-1}$.

peaks belonging to ITO are detected. Their peak positions remain unchanged during the whole sputter deposition process, indicating that the nanoscale structure of ITO remains intact during the TiO_x deposition. Similarly, also the SnO_2 nanoparticle film remains unchanged as seen from the unchanged related peak position. For the ITO- TiO_x sample, an additional small peak appears and continuously shifts to a lower q value when the effective thickness is above 4 nm, indicating the continuous growth of TiO_x microstructure [29]. Interestingly, another smaller peak appears and stays at the same q_y value after the thickness reaches 10 nm, which intensity increases with the thin film growth indicating the increasing amount of this structure. In contrast, for the SnO_2 - TiO_x sample, we find that the structure peak of TiO_x periodically changes during the sputter deposition, indicating the layer-by-layer growth of the TiO_x film.

To further understand the structure evolution of sputter-deposited TiO_x , we extract the TiO_x microstructure radius evolution for the ITO- TiO_x and SnO_2 - TiO_x samples from the model fits (Figs. 2c-2d). As already mentioned for the ITO- TiO_x sample, the radius (R) of the TiO_x microstructure (structure 1) grows continuously from 2.5 nm to 15.0 nm, and the center-to-center distance (D) equals twice the radius. After the effective thickness exceeds 10 nm, a smaller microstructure (structure 2) with a radius of about 2.5 nm appears, which radius remains unchanged with time [30]. For the SnO_2 - TiO_x sample, the radius of the TiO_x microstructure increases from about 2 nm to 5 nm. Then, the radius

undergoes another evolution, rising again from about 2 nm to 5 nm, followed by a next similar size evolution. This sequence implies that when the radius of TiO_x reaches 5 nm, the growth of the first layer is completed and fully covers the SnO_2 substrate. Then, the growth for the next layer and new islands commences with the continuous deposition process, which is followed by a third layer. Based on the *in situ* GISAXS observation results, a schematic diagram illustrating the TiO_x growth process on the ITO substrate and SnO_2 layer can be constructed (Figs. 2e-2f). In summary, the TiO_x microstructure exhibits conformal growth on both substrates via the Stranski-Krastanov growth mechanism which is in accordance with expectations from the literature for the growth of an oxide on another oxide [31], but the radius of the microstructure is larger on the ITO substrate than on the SnO_2 layer due to the template effect. Within an effective thickness of 30 nm, the TiO_x microstructure on top of the SnO_2 nanoparticle layer undergoes periodic evolution, resulting in a much smaller microstructure size compared with the TiO_x microstructure deposited on the ITO substrate. In addition, we use GISAXS and GIWAXS to simultaneously monitor the TiO_x thin film growth during sputter deposition. According to the *in situ* GIWAXS data, the sputter deposited TiO_x is not crystalline during sputter deposition (Fig. S4). Other mechanisms to explain the differences in the TiO_x particle size are the hydrophobic properties of the substrate and the interactions of TiO_x with ITO and SnO_2 . Compared with ITO, SnO_2 with a small water contact angle exhibits a stronger interaction with TiO_x [32,

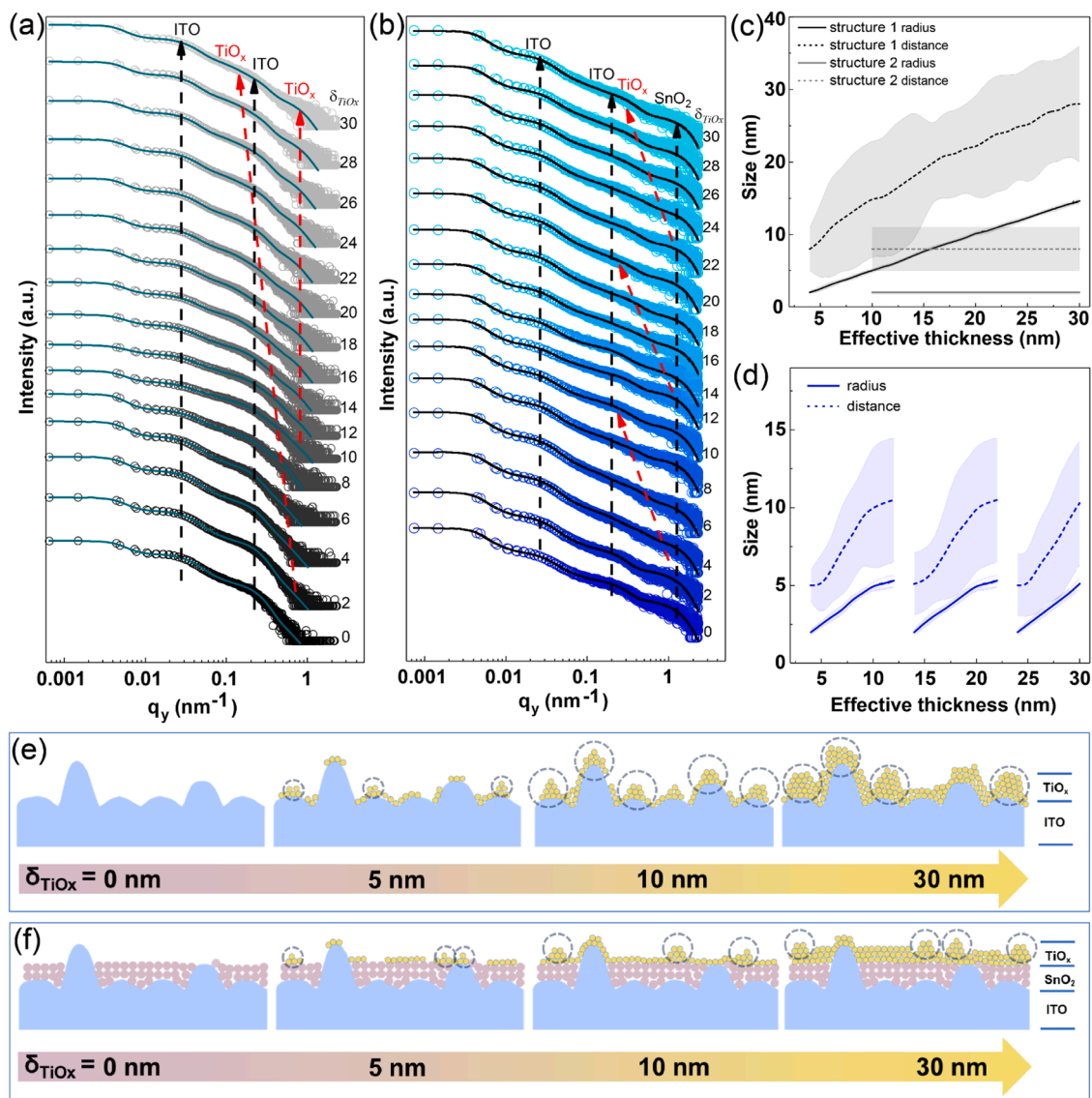


Fig. 2. Selected horizontal line cuts at different effective thicknesses for the a) pure ITO substrate and b) SnO₂ nanoparticle layer on ITO at a q_z region of 0.6–0.7 nm⁻¹. The circles refer to raw data and the corresponding fits are shown with solid lines, where the arrows indicate the structure evolution. For clarity of the presentation, the curves are shifted in vertical direction. Obtained microstructure radii (solid) and center-to-center distance (dashed) as a function of the effective TiO_x thickness for the c) pure ITO substrate and d) SnO₂ nanoparticle layer on ITO. Schematic diagram of the TiO_x thin film growth process on top of the e) pure ITO substrate and f) SnO₂ nanoparticle layer on ITO. The dashed circles represent the islands.

33], which prohibits the clusters from moving to grow into a large particle, resulting in small TiO_x particle sizes atop SnO₂ than atop the ITO substrate.

2.2. Characterization of sputtered TiO_x thin films

The performance of PSCs is strongly related to the morphology and properties of the HBL.¹³ To investigate the morphology of the TiO_x thin film atop the ITO and the SnO₂ layer, we measure top-view SEM of both samples before and after the sputter deposition (Figs. 3a–3d). As seen from the SEM images, when the effective thickness of the TiO_x layer is 30 nm, the diameter of the TiO_x microstructure atop the ITO substrate is about 30 nm in agreement with the GISAXS analysis. In comparison, the diameter of the TiO_x microstructure is about 10 nm atop the SnO₂ layer, which matches well with the GISAXS findings. A typically needed post-annealing treatment at 200°C for 30 min does not affect the structure of TiO_x (Fig. S5a–b) [34]. In addition, some bright particles can be seen for the SnO₂-coated ITO and SnO₂-TiO_x samples (thickness of 5 nm), which

are uncovered ITO grains with large heights (Fig. 3c and Fig. S5c). Fortunately for PSC applications, these non-conformal exposed ITO grains are fully covered by the sputter-deposited TiO_x thin layer when the effective thickness is higher or equal to 10 nm, resulting in a high-quality HBL layer (Fig. 3d and Fig. S5d). Such improved morphology with reduced defects is beneficial for the formation of a good interface contact and essential for reaching high PCE. The transmittance of the TiO_x layer is an essential factor for its application in PSCs. Despite the uncovered ITO issue that can be solved by increasing the thickness via the non-conformal growth spin-coating method, a too-thick hole-blocking layer introduced by spin-coating will inhibit electron extraction. In comparison, conformal growth TiO_x via sputter deposition only needs a very thin layer to fully cover the exposed ITO. Such thin layers not only ensure electron extraction and transport from the perovskite to the blocking layer but also reduce the surface roughness, which is beneficial for the perovskite growth. The digital pictures (Fig. 3e) show that the film color gets darker with increasing the TiO_x thickness, indicating that the TiO_x with insufficient amount of oxygen

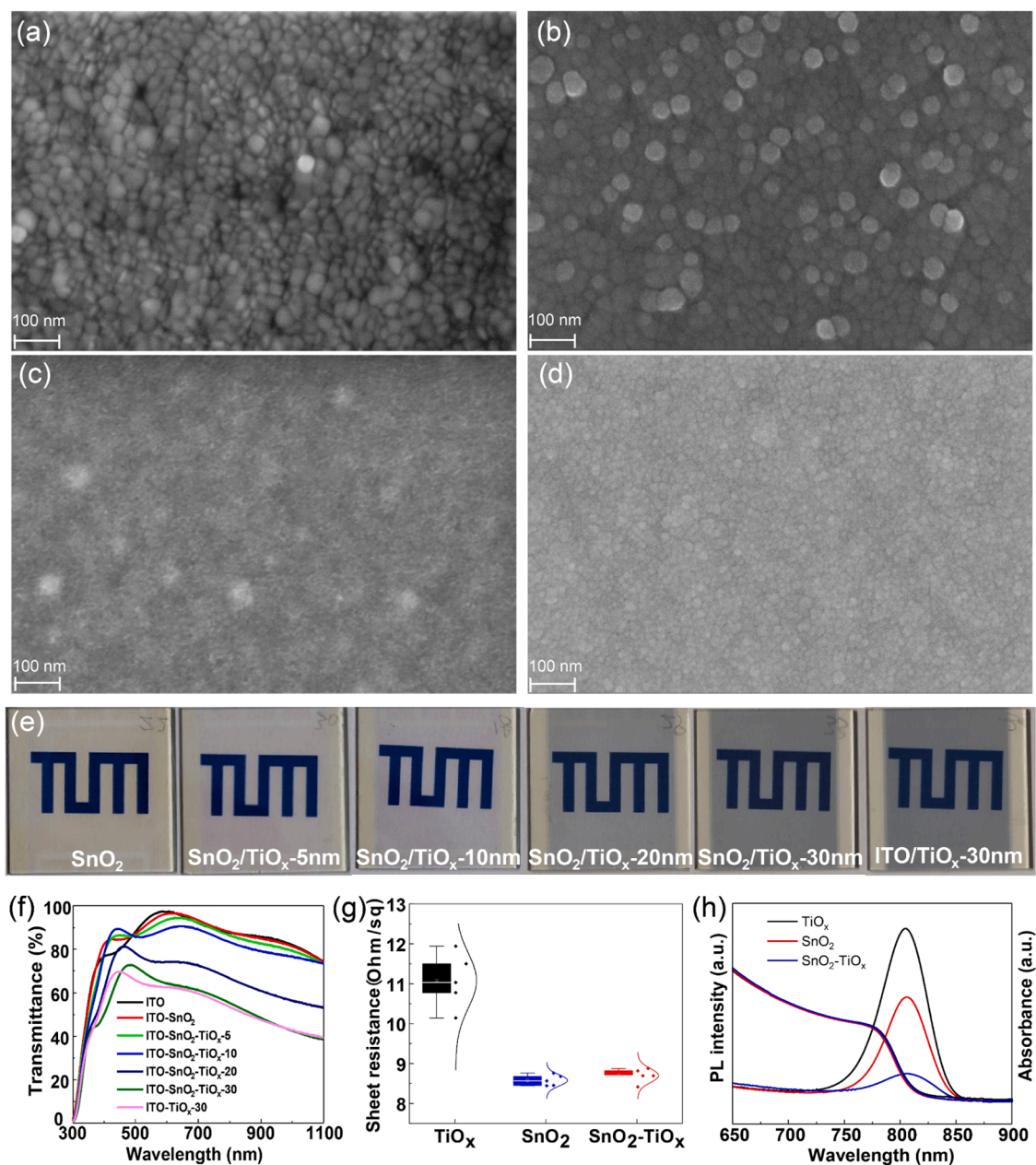


Fig. 3. Top view SEM images: a) before and b) after sputter deposition of 30 nm TiO_x on the pure ITO substrate, c) before and d) after sputter deposition of 30 nm TiO_x on the SnO₂ nanoparticle layer on ITO. e) Digital pictures of SnO₂-TiO_x samples with different effective TiO_x thicknesses and ITO-TiO_x samples with 30 nm TiO_x as labeled. f) UV-Vis transmittance spectra of ITO, ITO-TiO_x, and SnO₂-TiO_x with different effective TiO_x thicknesses. g) Sheet resistance for TiO_x, SnO₂, and SnO₂-TiO_x. h) Photoluminescence and UV-Vis spectra of TiO_x, SnO₂, and SnO₂-TiO_x samples with an ITO/HBL/perovskite structure.

exhibits partial absorption in the visible region. When the TiO_x thickness is above 10 nm, it is straightforward to distinguish the ITO substrate and the TiO_x area at the edge and the center, respectively. In the UV-Vis transmittance spectra (Fig. 3f), the transmittance decreases significantly when the TiO_x thickness is above 10 nm. After integrating the area of each curve in the transmittance spectra from 300 nm to 1100 nm (Fig. S6), the decrease in transmittance becomes very obvious when the thickness is above 10 nm. Such a low transmittance is detrimental for obtaining a high current density of PSCs [35]. Therefore, 10 nm thickness of the sputter-deposited TiO_x thin layer is regarded as the optimum thickness for the buried interface modification when using it in PSCs.

The conductivity of the HBL is a critical factor for its application in PSCs because it is highly related to the electron transport through the HBL [36]. A four-point probe method is used to measure the sheet resistance (R_S) of ITO, ITO-TiO_x, ITO/SnO₂, and ITO/SnO₂/TiO_x

samples. As seen in Fig. 3g, the TiO_x film exhibits the highest average R_S value, indicating the lowest electron transport ability. The SnO₂ nanoparticle layer on ITO reduces the average R_S value, which shows that the additional layer is beneficial. After the modification with a sputter-deposited TiO_x thin film, the sheet resistance value remains almost unchanged, indicating a similar level of conductivity between SnO₂ and SnO₂-TiO_x. The non-radiative recombination caused by interface defects is a crucial factor limiting the open circuit voltage in PSCs [37]. To investigate that, we perform a steady-state photoluminescence (PL) measurement of a two-step spin-coated perovskite thin film atop the TiO_x, SnO₂, and SnO₂-TiO_x samples. As shown in Fig. 3h, all samples show a typical FA_{1-x}Cs_xPbI₃ perovskite emission peak at about 806 nm. Interestingly, TiO_x-perovskite shows a higher PL intensity than SnO₂-perovskite, while the SnO₂-TiO_x-perovskite film exhibits the lowest intensity. The decreased PL intensity is attributed to

the better interface contact and fewer defects at the buried interface, which can facilitate the charge carrier transport from perovskite to HBL, such that it reduces the charge carrier number for radiative recombination [38]. The different kinds of HBLs do not affect the perovskite absorption properties and bandgap because all curves are almost entirely overlapping in the UV-Vis spectra and the Tauc plot analysis (Fig. S7). According to the literature and our previous reports, the conduction band of TiO_x , SnO_2 , ITO, and $\text{FA}_{0.85}\text{MA}_{0.1}\text{Cs}_{0.05}\text{PbI}_3$ perovskite is at -4.1 eV, -4.3 eV, -4.6 eV, and -4.09 eV, respectively [39–42]. As shown in Fig. S8, such cascade band energy alignment will be beneficial for electron extraction and transport.

2.3. Photovoltaic performance of PSCs

Based on the in-situ observation of TiO_x thin film growth and the material characterization of TiO_x thin films, we decide to use the 10 nm TiO_x as a buried interface modification layer on the SnO_2 ($\text{SnO}_2\text{-TiO}_x$) HBL for PSCs to investigate its effect on the device performance. For comparison, a 30 nm pure TiO_x layer is also applied in PSCs as HBL to demonstrate its potential in device performance compared to the normal SnO_2 HBL. A regular ITO/HBL/perovskite/F-PEAI/spiro-OMeTAD/Au device structure is used in this work (Fig. S9). Fig. 4a shows the PCE distribution for 8 TiO_x , SnO_2 , and $\text{SnO}_2\text{-TiO}_x$ devices, respectively. Among the three kinds of devices, the TiO_x -based devices show the lowest average PCE (15.4 %) and the widest statistic distribution of PCE values. As expected, the average PCE of a SnO_2 -based device is improved after the buried interface modification via a sputter-deposited TiO_x thin layer on the HBL (from 22.19 % to 23.93 %). Similarly, the same trend can be seen in the current density-voltage (J - V) curves and photovoltaic

parameters of the champion device based on TiO_x , SnO_2 , and $\text{SnO}_2\text{-TiO}_x$ (Figs. 4b-4d and Table 1). The champion TiO_x -based device exhibits a PCE of 17.32 %, a fill factor (FF) of 70.87 %, a V_{OC} of 1.067 V, and a J_{SC} of 22.91 mA cm^{-2} by reverse scanning, which is far behind the SnO_2 -based device with a PCE of 22.19 %, an FF of 82.55 %, a V_{OC} of 1.094 V, and a J_{SC} of 24.57 mA cm^{-2} . This significant difference is attributed to the insufficient transmittance and poor conductivity of the pure sputter-deposited TiO_x layer and poor interface contact with the perovskite layer. In comparison, the $\text{SnO}_2\text{-TiO}_x$ -based device performs better than the SnO_2 -based device with a PCE of 23.93 %, an FF of 81.41 %, a V_{OC} of 1.177 V, and a J_{SC} of 24.97 mA cm^{-2} . The PCE improvement is mainly attributed to the significant increase in V_{OC} value. The slight increase in current density comes from better interface contact, improved charge transfers, and enhanced charge extraction capacity [21,26]. As expected, the buried interface modification via a sputter-deposited TiO_x thin layer improves the photovoltaic performance due to the better

Table 1

The photovoltaic parameters of the champion device for TiO_x , SnO_2 , and $\text{SnO}_2\text{-TiO}_x$ samples.

Device	Direction	V_{OC} (V)	J_{SC} (mA cm^{-2})	FF (%)	PCE (%)
TiO_x	forward	1.061	22.61	61.04	14.64
	reverse	1.067	22.91	70.87	17.32
SnO_2	forward	1.085	24.54	82.63	22.00
	reverse	1.094	24.57	82.55	22.19
$\text{SnO}_2\text{-TiO}_x$	forward	1.177	24.97	80.99	23.80
	reverse	1.177	24.97	81.41	23.93

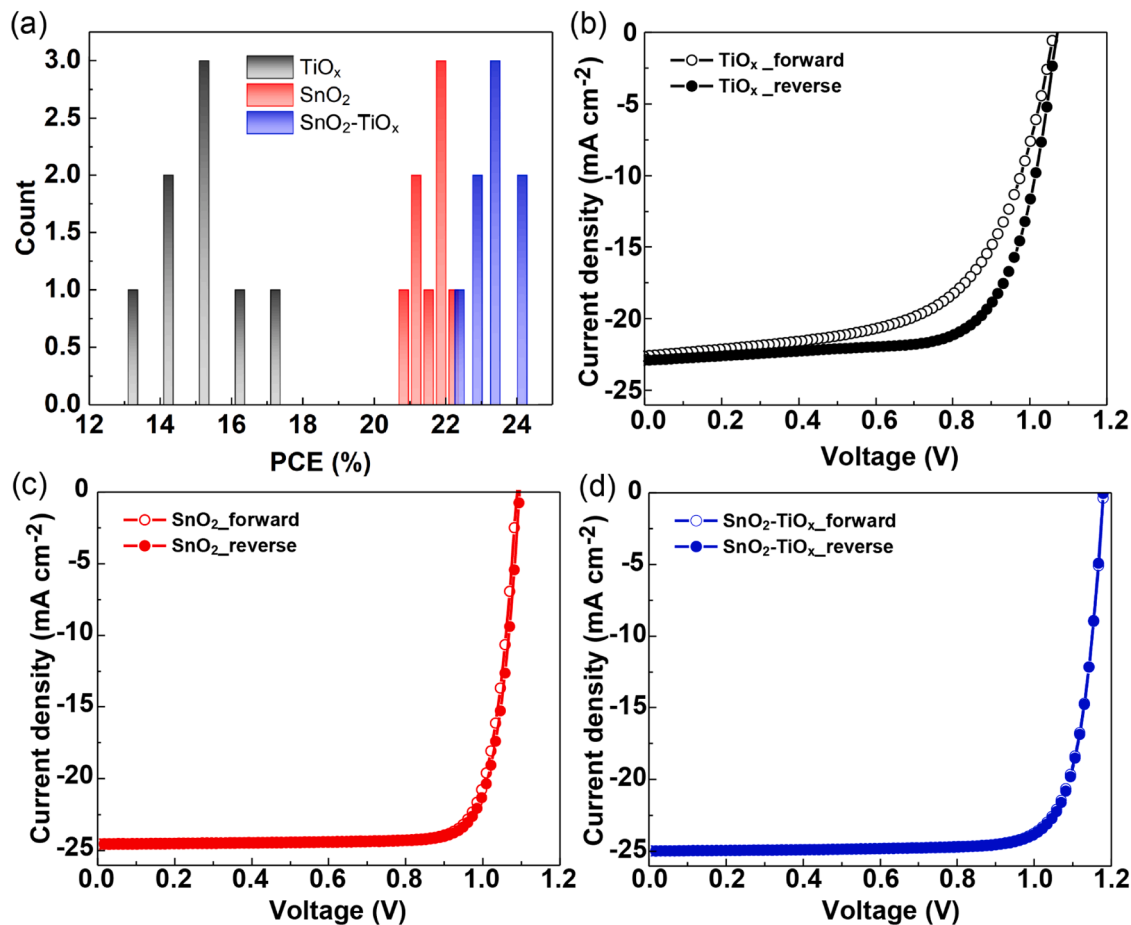


Fig. 4. a) Bar chart of PCE obtained from 8 devices for TiO_x , SnO_2 , and $\text{SnO}_2\text{-TiO}_x$ samples. J - V curves with forward and reverse scans from -0.2 V to 1.2 V of the champion device for b) TiO_x , c) SnO_2 , and d) $\text{SnO}_2\text{-TiO}_x$ samples.

interface contact and the reduced trap density at the buried interface, suppressing the non-radiative recombination [43]. The performance of the $\text{SnO}_2\text{-TiO}_x\text{-5 nm}$ device is between the pure SnO_2 device and the $\text{SnO}_2\text{-TiO}_x\text{-10 nm}$ device, with a reverse scan PCE of 22.41 %, a V_{OC} of 1.108 V, a J_{SC} of 24.68 mA cm^{-2} , and an FF of 81.95 % (Fig. S10a). In addition, the performance of the $\text{SnO}_2\text{-30 nm}$ device is lower than the $\text{SnO}_2\text{-20 nm}$ device, with a reverse scan PCE of 21.92 % (Fig. S10b). This finding can be attributed to the slight decrease in electron extraction and transport capacity for higher thicknesses of the SnO_2 layer.

2.4. Operational stability of PSCs

The operational device stability is still a limitation for the daily life use of PSCs and *operando* GIWAXS is a powerful technique to understand the aging of PSCs during operation. This work uses a home-built setup (Fig. S11) to measure the $J\text{-}V$ curve of all samples under a nitrogen atmosphere and one-sun solar illumination (ISOS-L-11) simultaneously

with GIWAXS. The evolution of photovoltaic parameters for TiO_x -, SnO_2 -, and $\text{SnO}_2\text{-TiO}_x$ -based devices is shown in Figs. 5a-5c (normalized from five devices). The TiO_x -based device offers the worst stability compared with SnO_2 -based and $\text{SnO}_2\text{-TiO}_x$ -based devices due to having an insufficient HBL. All photovoltaic parameters of TiO_x -based decrease dramatically, especially the PCE, showing a reduction of 50 % after 120 min of operation. The loss in PCE is driven by the decrease in J_{SC} . In contrast, for the $\text{SnO}_2\text{-TiO}_x$ -based devices, the V_{OC} and J_{SC} values remain at 98 % of their initial value, while the FF shows a decrease of 23 %, resulting in a PCE decrease of 25 %, which is much smaller than the 45 % of the SnO_2 -based device. Thus, the buried interface modification via a sputter-deposited TiO_x thin layer improves significantly the operation stability. For the SnO_2 -based and $\text{SnO}_2\text{-TiO}_x$ -based devices, the FF decrease is driving the degradation.

The understanding of the structure change during the operation process is gained from the *operando* GIWAXS study. Before the *operando* measurements, an X-ray irradiation damage test is conducted to exclude

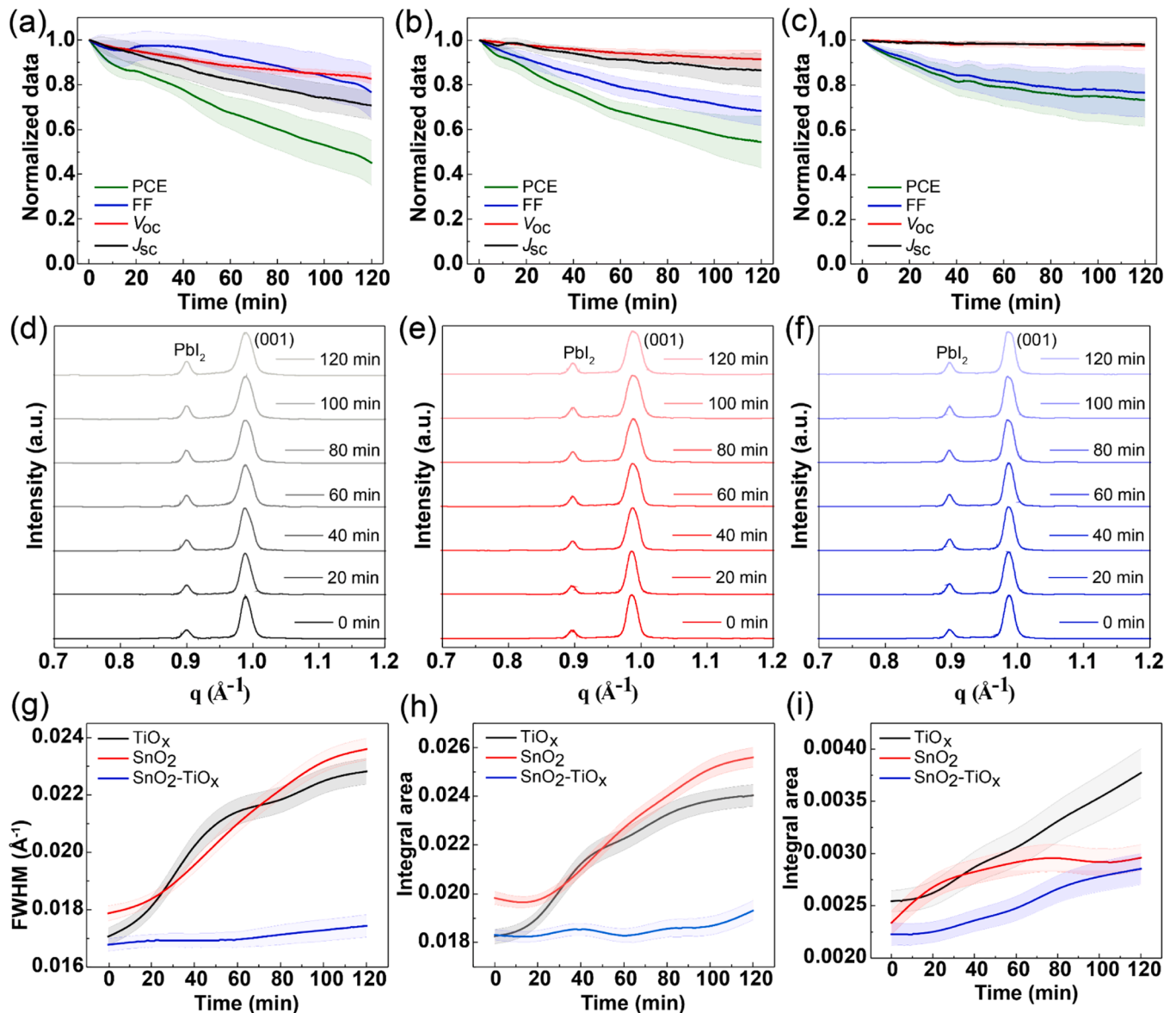


Fig. 5. Temporal evolution of PCE, FF, V_{OC} , and J_{SC} measured by the reverse scan from -0.2 V to 1.2 V for a) TiO_x , b) SnO_2 , and c) $\text{SnO}_2\text{-TiO}_x$ based PSCs under nitrogen. The shaded area refers to the error bars derived from the standard deviation of normalized PCE, J_{SC} , V_{OC} , and FF values of five devices. Evolution of enlarged-range pseudo-XRD data (q region of $0.7\text{-}1.2 \text{ \AA}^{-1}$) during the operation of d) TiO_x , e) SnO_2 , and f) $\text{SnO}_2\text{-TiO}_x$ based PSCs. Evolution of g) full width at half maximum (FWHM), h) integral areas of (001) Bragg peak of perovskite crystal, and i) integral areas of the PbI_2 Bragg peak during *operando* measurement for TiO_x , SnO_2 , and $\text{SnO}_2\text{-TiO}_x$ based PSCs.

that the perovskite structure changes are caused by the X-ray beam (Fig. S12) [44]. The typical scatter signals of the perovskite crystal and of the residual PbI_2 can be seen from the selected 2D GIWAXS data (Fig. S13). For the further investigation of the structure changes, the radial GIWAXS profiles integrated over all azimuth angles (pseudo-XRD data) are plotted in Fig. S14, which are corrected based on the peak of the ITO substrate. The enlarged pseudo-XRD spectra are plotted in Figs. 5d-5f to clearly show the structure evolution. There is no peak position shift or splitting of the (001) Bragg peaks for all samples, indicating there is no detectable phase segregation in the perovskite [45]. However, the full width at half maximum (FWHM) of the (001) Bragg peaks broadens continuously during operation (Fig. 5g) [46]. The FWHM of TiO_x -based and SnO_2 -based devices show a similar increased value (0.023 and 0.024, respectively) which are much higher than in case of the SnO_2 - TiO_x -based devices (0.017). The broadening of the (001) Bragg peak originates from a tensile strain due to the device operation. The integral area of the (001) perovskite Bragg peaks (Fig. 5h) shows a similar evolution driven as the FWHM increase, indicating that the SnO_2 - TiO_x -based devices exhibit the lowest crystallinity decrease [47]. For the PbI_2 peak, it is not the increase in FWHM but the increase in intensity driving the behavior of the integral area, as shown in Fig. 5i. Thus, PbI_2 is not strained but generated during the device operation. Despite the integral area increasing continuously in all devices, the SnO_2 - TiO_x -based device exhibits the lowest increase during the whole *operando* study. The higher integral area means that more PbI_2 is present in the perovskite layer, indicating a higher perovskite decomposition [48]. The TiO_x -based devices exhibit the strongest formation of PbI_2 in agreement with the worst device stability. Comparing the SnO_2 -based and SnO_2 - TiO_x -based devices, in particular in the early device operation (first 100 min), without the interface modification significantly more PbI_2 is formed causing the faster aging. Thus, the improvement in stability after interface modification is attributed to the reduction of defect density at the buried interface, which prevents the formation of PbI_2 [49,50].

We further investigate the microstrain evolution by the Williamson-Hall analysis applied to the pseudo-XRD data [44]. During the first 20 min of operation, the microstrain in the active layer of TiO_x -based and SnO_2 -based devices is slightly released, followed by a continuous increase to the initial level (Fig. S15d-15e). In contrast, for the SnO_2 - TiO_x -based device, the microstrain in the active layer is continuously released during the first 60 min of operation and then remains constant with slight fluctuations (Fig. S15f). Such microstrain relaxation of the active layer is beneficial for slowing down the crystal structure degradation and a related PCE decrease.

3. Conclusion

With the *in situ* GISAXS measurements during sputter deposition, the TiO_x thin film growth process on top of a pure ITO substrate and a SnO_2 nanoparticle layer on ITO is compared, and the microstructure evolution of TiO_x via the Stranski-Krastanov growth mechanism is clarified. The template effects of the SnO_2 nanoparticles primarily affect the microstructure growth and evolution, giving rise to the presence of a smaller TiO_x microstructure atop the SnO_2 nanoparticles layer compared to the TiO_x microstructure atop the ITO substrate. The pure TiO_x layer atop the ITO substrate exhibits poor optical and electrical properties, while the optical and electrical properties are preserved for the sputter-deposited TiO_x thin layer (10 nm) atop the SnO_2 nanoparticles layer. The buried interface modification introduced via a sputter-deposited 10 nm TiO_x thin layer has a beneficial effect on improving PSC photovoltaic performance and stability due to its better interface contact and suppressed non-radiative recombination at the buried interface of the perovskite layer. The *operando* GIWAXS study demonstrates that the buried interface modification via a sputter-deposited TiO_x thin layer slows down the perovskite decomposition process and the detrimental formation of PbI_2 . Thus, sputter deposition of a 10 nm TiO_x thin layer improves the SnO_2

nanoparticle-based HBL, which is commonly used in PSCs concerning the PCE and in particular with respect to the device stability.

4. Experimental section

4.1. Materials

DMF, DMSO, lead iodide (PbI_2), cesium iodide (CsI), formamidinium iodide (FAI), methylammonium iodide (MAI), methylammonium chloride (MACl), spiro-OMeTAD, isopropanol (IPA), chlorobenzene (CB), acetonitrile (ACN), 4-tert-butyl pyridine, and lithium bis(trifluoromethanesulfonyl)imide (Li-TFSI) were purchased from Sigma-Aldrich. 4-fluoro-phenethylammonium iodide (F-PEAI) was purchased from GreatCell Solar (Dyesol Ltd). SnO_2 colloidal solution (15 wt% in water) was purchased from Alfa Aesar. All materials were used directly without further purification.

4.2. Sputter deposition

A DC magnetron sputter setup was applied to realize the sputter deposition of TiO_x via a reactive sputtering method. The optimization of sputter parameters, including power, Ar/O_2 ratio, gas flow, and pressure, was done in pre-tests and will be beyond the scope of the present study, which focuses on the optimal parameters as provided in the text. The optimization of TiO_x thickness was conducted by sputter depositing 5 nm, 10 nm, 20 nm, and 30 nm of TiO_x thin film on top of the SnO_2 layer, and we found that 10 nm of TiO_x is the optimal thickness. Sputtering parameters were: power $P = 47$ W, chamber pressure without gas flow $p_c = 3 \times 10^{-6}$ mbar, chamber pressure during sputter $p_{cs} = \sim 0.35$ Pa, argon flow $f_a = 10$ sccm, and oxygen flow $f_o = 0.27$ sccm. The deposition rate (J) was estimated to be *ca.* 0.5 \AA s^{-1} based on a quartz crystal microbalance (QCM) mounted on the shutter. A pneumatic sample shutter was used to control the start and end of the sputtering process. After sputter deposition, the TiO_x thin films were annealed at 200°C for 30 min for better crystallinity and conductivity.

4.3. In situ GISAXS measurement

To observe the growth process of the sputter-deposited TiO_x thin film, the sputter deposition setup was integrated into a synchrotron-based grazing-incidence small-angle scattering (GISAXS) setup at P03/MiNaXS beamline of the PETRA III storage ring at Deutsches Elektronen-Synchrotron (DESY, Hamburg, Germany). The wavelength of the X-ray was 1.048 \AA , corresponding to a photon energy of 11.74 keV . The sample-to-sample distance (SDD) was set as 3415 mm . During the *in situ* measurement, an incidence angle (α_i) of 0.4 degrees was applied, which was higher than the critical angle of TiO_2 (0.2°). A 2D detector of Pilatus 2 M (Dectris Ltd., Switzerland; pixel size = $172 \times 172 \text{ \mu m}^2$) was used to continuously collect the 2D scattering patterns with a time resolution of 0.05 s (20 images per second). The sample was moved along the y-axis direction within a selected homogeneous region during the *in situ* GISAXS measurement to avoid possible sample damage under X-ray radiation. The GISAXS data were analyzed via the software DPDAK [51]. Then, the horizontal line cut data were modeled based on the distorted wave Born approximation framework.

4.4. Device fabrication

The ITO glass substrates were washed with acetone, 2-propanol (IPA), and ethanol via an ultrasonic cleaner for 20 min each step. Then, the substrates were dried with nitrogen gas flow. Before spin-coating, the ITO substrates were treated with plasma cleaning for 15 min. The SnO_2 layer was fabricated by spin-coat a diluted SnO_2 nanoparticle solution (3 wt% in water) atop ITO substrates at 4000 rpm for 30 s and then annealing at 150°C for 30 min. The perovskite precursor of $\text{FA}_{0.85}\text{MA}_{0.1}\text{Cs}_{0.05}\text{PbI}_3$ with 30 mg of MACl (1.6 M

concentration in a 4:1 mixture of DMF and DMSO) was then spin-coated onto the substrates at 5000 rpm for 50 s, a 200 μL solution of CB dropped quickly at the 15th second of the spin-coating process. Then, the perovskite films were annealed at 100 $^{\circ}\text{C}$ for 30 min in ambient air with relative humidity (RH) < 30 %. The passivation layer was spin-coated at 4000 rpm for 30 s (3.0 mg of F-PEAI in 1 mL of IPA). After that, the spiro-OMeTAD was spin-coated atop the perovskite layer at 4000 rpm for 30 s. The spiro-OMeTAD solution was prepared by mixing 72.3 mg spiro-OMeTAD, 30 μL bis(trifluoromethane) sulfonimide lithium salt (Li-TFSI) stock solution (260 mg Li-TFSI in 1 mL acetonitrile), and 29 μL 4-tertbutylpyridine in 1 mL chlorobenzene [52]. After that, the samples were stored in a sealed box with humidity lower than 10 % for 8 h to oxidize spiro-OMeTAD. Finally, 80 nm of a gold electrode was fabricated via evaporation with a six-pixel sample holder. The effective area of each pixel is about 0.2 cm^2 . A mask with 0.08 cm^2 .

4.5. Operando GIWAXS measurement

The *operando* grazing-incidence wide-angle X-ray scattering (GIWAXS) measurements were carried out at the P03/MiNaXS beamline of the PETRA III storage ring at DESY. A LAMBDA 9 M detector collected the GIWAXS data. The photon energy of the X-ray was 11.79 keV, corresponding to a wavelength of 1.044 \AA . The sample-to-sample distance (SDD) was set as 163.5 mm. An incidence angle (α_i) of 0.8 degrees was applied to enable the interaction between the X-ray and ITO substrate. The software INSIGHT was used to conduct the data analysis [53]. Due to the thermal expansion under light illumination, the SDD must be corrected based on the ITO substrate signal at $q = 2.139 \text{\AA}^{-1}$ [44]. During the *operando* measurement, the current density-voltage (J - V) curves were measured under the illumination of 150 Watts Xenon short-arc lamps (PE150AF, Excelitas Technologies), with initial UV output (<390 nm, total output in all directions) is 0.9 Watts.

4.6. Characterization

The top-view and cross-section SEM images were collected by scanning electron microscopy (Zeiss Gemini NVision 40) with an electron high tension (EHT) voltage of 5 keV and a working distance of 5.3 mm. A Perkin Elmer Lambda 35 was used to measure the UV-Vis spectra with a scan speed of 480 nm min^{-1} . The sheet resistance was measured by a four-point probe setup with a Keithley 2400 source meter. The photoluminescence (PL) spectra were collected by PerkinElmer LS 55 fluorescence spectrometer under a 450 nm excitation laser. The J - V measurement was conducted under AM 1.5 G illumination (100 W/m^2) by a solar simulator assembled with a Keithley 2611B source meter. A Si reference cell (Fraunhofer ISE019–2015) was used to calibrate the light intensity of a solar simulator.

CRedit authorship contribution statement

Zerui Li: Writing – review & editing, Methodology, Investigation, Formal analysis, Data curation. **Stephan V. Roth:** Writing – review & editing, Supervision, Resources, Funding acquisition. **Kun Sun:** Writing – review & editing, Methodology, Investigation, Formal analysis, Data curation. **Franz Faupel:** Writing – review & editing, Supervision, Resources, Funding acquisition. **Thomas Strunskus:** Writing – review & editing, Methodology, Investigation, Formal analysis, Data curation. **Jie Zeng:** Writing – review & editing, Methodology, Investigation, Formal analysis, Data curation. **Xiongzhuo Jiang:** Writing – original draft, Validation, Methodology, Investigation, Formal analysis, Data curation, Conceptualization. **Kristian A. Reck:** Writing – review & editing, Methodology, Investigation, Formal analysis, Data curation. **Matthias Schwartzkopf:** Writing – review & editing, Methodology, Investigation. **Benedikt Sochor:** Writing – review & editing, Investigation, Formal analysis, Data curation. **Yusuf Bulut:** Writing – review & editing, Investigation, Formal analysis, Data curation. **Suzhe Liang:** Writing –

review & editing, Visualization, Methodology, Investigation, Formal analysis, Data curation. **Renjun Guo:** Writing – review & editing, Validation, Methodology, Investigation, Formal analysis, Data curation. **Guangjiu Pan:** Writing – review & editing, Methodology, Investigation, Formal analysis, Data curation. **Peter Mueller-Buschbaum:** Writing – review & editing, Supervision, Resources, Project administration, Funding acquisition, Conceptualization. **Zhuijun Xu:** Writing – review & editing, Methodology, Investigation, Formal analysis, Data curation. **Baomin Xu:** Writing – review & editing, Supervision, Resources, Funding acquisition.

Declaration of Competing Interest

The authors declare that they have no known competing financial interests or personal relationships that could have appeared to influence the work reported in this paper

Acknowledgments

This work was supported by funding from the Deutsche Forschungsgemeinschaft (DFG, German Research Foundation) with funding via projects RO 4638/3–1, FA 234/36–1, and MU 1487/39–1, by Germany's Excellence Strategy - EXC 2089/1–390776260 (e-conversion), TUM.solar in the context of the Bavarian Collaborative Research Project Solar Technologies Go Hybrid (SolTech), the Center for NanoScience (CeNS) and the International Research Training Group 2022 Alberta/Technical University of Munich International Graduate School for Environmentally Responsible Functional Hybrid Materials (ATUMS). X. Jiang, K. Sun, Z. Li, G. Pan, and S. Liang acknowledge the financial support from the China Scholarship Council (CSC). Parts of this research were carried out at the P03 beamline of PETRAIII at DESY, a member of the Helmholtz Association HGF.

Appendix A. Supporting information

Supplementary data associated with this article can be found in the online version at [doi:10.1016/j.nanoen.2024.110360](https://doi.org/10.1016/j.nanoen.2024.110360).

Data Availability

Data will be made available on request.

References

- [1] H.S. Jung, N.-G. Park, Perovskite solar cells: from materials to devices, *Small* 11 (2015) 10–25, <https://doi.org/10.1002/smll.201402767>.
- [2] J. Guo, B. Wang, D. Lu, T. Wang, T. Liu, R. Wang, X. Dong, T. Zhou, N. Zheng, Q. Fu, Z. Xie, X. Wan, G. Xing, Y. Chen, Y. Liu, Ultralong carrier lifetime exceeding 20 μs in lead halide perovskite film enable efficient solar cells, *Adv. Mater.* 35 (2023) 2212126, <https://doi.org/10.1002/adma.202212126>.
- [3] A. Kojima, K. Teshima, Y. Shirai, T. Miyasaka, Organometal halide perovskites as visible-light sensitizers for photovoltaic cells, *J. Am. Chem. Soc.* 131 (2009) 6050–6051, <https://doi.org/10.1021/ja809598r>.
- [4] N.R.E.L. (NREL), Best Research-Cell Efficiency Chart, (accessed June 2024).
- [5] W. Shockley, H. Queisser, Detailed balance limit of efficiency of p–n junction solar cells, in: *Renew. Energ.*, Routledge, 2018, pp. 35–54.
- [6] Y. Zhang, Y. Liu, S. Liu, Composition engineering of perovskite single crystals for high-performance optoelectronics, *Adv. Funct. Mater.* 33 (2023) 2210335, <https://doi.org/10.1002/adfm.202210335>.
- [7] R. Liu, K. Xu, Solvent engineering for perovskite solar cells: a review, *Micro-Nano Lett.* 15 (2020) 349–353, <https://doi.org/10.1049/mnl.2019.0735>.
- [8] X. Cai, T. Hu, H. Hou, P. Zhu, R. Liu, J. Peng, W. Luo, H. Yu, A review for nickel oxide hole transport layer and its application in halide perovskite solar cells, *Mater. Today Sustain.* 23 (2023) 100438, <https://doi.org/10.1016/j.mtsust.2023.100438>.
- [9] X. Jiang, S. Chen, Y. Li, L. Zhang, N. Shen, G. Zhang, J. Du, N. Fu, B. Xu, Direct surface passivation of perovskite film by 4-fluorophenethylammonium iodide toward stable and efficient perovskite solar cells, *ACS Appl. Mater. Interfaces* 13 (2021) 2558–2565, <https://doi.org/10.1021/acsami.0c17773>.
- [10] Z.W. Gao, Y. Wang, W.C. Choy, Buried interface modification in perovskite solar cells: a materials perspective, *Adv. Energy Mater.* 12 (2022) 2104030, <https://doi.org/10.1002/aenm.202104030>.

- [11] J. Gong, Y. Cui, F. Li, M. Liu, Progress in surface modification of SnO₂ electron transport layers for stable perovskite solar cells, *Small Sci.* 3 (2023) 2200108, <https://doi.org/10.1002/smssc.202200108>.
- [12] M.F.M. Noh, C.H. Teh, R. Daik, E.L. Lim, C.C. Yap, M.A. Ibrahim, N.A. Ludin, A.R. bin Mohd Yusoff, J. Jang, M.A.M. Teridi, The architecture of the electron transport layer for a perovskite solar cell, *J. Mater. Chem. C* 6 (2018) 682–712, <https://doi.org/10.1039/C7TC04649A>.
- [13] S.Y. Park, K. Zhu, Advances in SnO₂ for efficient and stable n–i–p perovskite solar cells, *Adv. Mater.* 34 (2022) 2110438, <https://doi.org/10.1002/adma.202110438>.
- [14] L. Huang, Y.H. Lou, Z.K. Wang, Buried interface passivation: a key strategy to breakthrough the efficiency of perovskite photovoltaics, *Small* (2023) 2302585, <https://doi.org/10.1002/smll.202302585>.
- [15] Z. Ni, C. Bao, Y. Liu, Q. Jiang, W.-Q. Wu, S. Chen, X. Dai, B. Chen, B. Hartweg, Z. Yu, Z. Holman, J. Huang, Resolving spatial and energetic distributions of trap states in metal halide perovskite solar cells, *Science* 367 (2020) 1352–1358, <https://doi.org/10.1126/science.aba089>.
- [16] D. Luo, R. Su, W. Zhang, Q. Gong, R. Zhu, Minimizing non-radiative recombination losses in perovskite solar cells, *Nat. Rev. Mater.* 5 (2020) 44–60, <https://doi.org/10.1038/s41578-019-0151-y>.
- [17] K. Sun, P. Müller-Buschbaum, Shedding light on the moisture stability of halide perovskite thin films, *Energy Technol.* 11 (2023) 2201475, <https://doi.org/10.1002/ente.202201475>.
- [18] A. Uddin, H.J.S.R. Yi, Progress and challenges of SnO₂ electron transport layer for perovskite solar cells: A critical review, *Sol. RRL* 6 (2022) 2100983, <https://doi.org/10.1002/solr.202100983>.
- [19] W.L. Lachore, D.M. Andoshe, M.A. Mekonnen, F.G. Hone, Recent progress in electron transport bilayer for efficient and low-cost perovskite solar cells: a review, *J. Solid State Electrochem.* 26 (2022) 295–311, <https://doi.org/10.1007/s10008-021-05064-z>.
- [20] M.M. Tavakoli, P. Yadav, R. Tavakoli, J. Kong, Surface engineering of TiO₂ ETL for highly efficient and hysteresis-less planar perovskite solar cell (21.4%) with enhanced open-circuit voltage and stability, *Adv. Energy Mater.* 8 (2018) 1800794, <https://doi.org/10.1002/aenm.201800794>.
- [21] H. Shu, C. Peng, Q. Chen, Z. Huang, C. Deng, W. Luo, H. Li, W. Zhang, W. Zhang, Y. Huang, Strategy of enhancing built-in field to promote the application of C-TiO₂/SnO₂ bilayer electron transport layer in high-efficiency perovskite solar cells (24.3%), *Small* 18 (2022) 2204446, <https://doi.org/10.1002/smll.202204446>.
- [22] M.J. Paik, J.W. Yoo, J. Park, E. Noh, H. Kim, S.-G. Ji, Y.Y. Kim, S.I. Seok, SnO₂-TiO₂ hybrid electron transport layer for efficient and flexible perovskite solar cells, *ACS Energy Lett.* 7 (2022) 1864–1870, <https://doi.org/10.1021/acscenergylett.2c00637>.
- [23] F. Xie, D. Mei, L. Qiu, Z. Su, L. Chen, Y. Liu, P. Du, High-Efficiency Fiber-Shaped Perovskite Solar Cells with TiO₂/SnO₂ Double-Electron Transport Layer Materials, *J. Electron. Mater.* 52 (2023) 4626–4633, <https://doi.org/10.1007/s11664-023-10429-3>.
- [24] H. Xie, X. Yin, J. Liu, Y. Guo, P. Chen, W. Que, G. Wang, B. Gao, Low temperature solution-derived TiO₂-SnO₂ bilayered electron transport layer for high performance perovskite solar cells, *Appl. Surf. Sci.* 464 (2019) 700–707, <https://doi.org/10.1016/j.apsusc.2018.09.146>.
- [25] G. Martínez-Denegri, S. Colodrero, M. Kramarenko, J. Martorell, All-Nanoparticle SnO₂/TiO₂ Electron-Transporting Layers Processed at Low Temperature for Efficient Thin-Film Perovskite Solar Cells, *ACS Appl. Energy Mater.* 1 (2018) 5548–5556, <https://doi.org/10.1021/acsaem.8b01118>.
- [26] M. Hu, L. Zhang, S. She, J. Wu, X. Zhou, X. Li, D. Wang, J. Miao, G. Mi, H. Chen, Y. Tian, B. Xu, C. Cheng, Electron transporting bilayer of SnO₂ and TiO₂ nanocolloid enables highly efficient planar perovskite solar cells, *Sol. RRL* 4 (2020) 1900331, <https://doi.org/10.1002/solr.201900331>.
- [27] J.B. Bellam, G. Kandikunta, B. Manupati, S. Debabrata, P.P. George, S. Victor Vedanayakam, V.K. Verma, DC sputter deposited TiO₂ thin film on ITO/glass substrate for perovskite solar cell application, *Mater. Today: Proc.* 45 (2021) 3886–3890, <https://doi.org/10.1016/j.matpr.2020.06.281>.
- [28] A. Alberti, E. Smecca, S. Sanzaro, C. Bongiorno, F. Giannazzo, G. Mannino, A. La Magna, M. Liu, P. Vivo, A. Listorti, E. Calabrò, F. Matteocci, A. Di Carlo, Nanostructured TiO₂ grown by low-temperature reactive sputtering for planar perovskite solar cells, *ACS Appl. Energy Mater.* 2 (2019) 6218–6229, <https://doi.org/10.1021/acsaem.9b00708>.
- [29] S. Liang, W. Chen, S. Yin, S.J. Schaper, R. Guo, J. Drewes, N. Carstens, T. Strunskus, M. Gensch, M. Schwartzkopf, F. Faupel, S.V. Roth, Y.-J. Cheng, P. Müller-Buschbaum, Tailoring the optical properties of sputter-deposited gold nanostructures on nanostructured titanium dioxide templates based on in situ grazing-incidence small-angle X-ray scattering determined growth laws, *ACS Appl. Mater. Interfaces* 13 (2021) 14728–14740, <https://doi.org/10.1021/acsaem.1c00972>.
- [30] W. Chen, S. Liang, F.C. Löhner, S.J. Schaper, N. Li, W. Cao, L.P. Kreuzer, H. Liu, H. Tang, V. Körstgens, M. Schwartzkopf, K. Wang, X.W. Sun, S.V. Roth, P. Müller-Buschbaum, In situ grazing-incidence small-angle X-ray scattering observation of gold sputter deposition on a PbS quantum dot solid, *ACS Appl. Mater. Interfaces* 12 (2020) 46942–46952, <https://doi.org/10.1021/acsaem.0c12732>.
- [31] K. Płacheta, A. Kot, J. Banas-Gac, M. Zając, M. Sikora, M. Radecka, K. Zakrzewska, Evolution of surface properties of titanium oxide thin films, *Appl. Surf. Sci.* 608 (2023) 155046, <https://doi.org/10.1016/j.apsusc.2022.155046>.
- [32] S. You, H. Zeng, Z. Ku, X. Wang, Z. Wang, Y. Rong, Y. Zhao, X. Zheng, L. Luo, L. Li, S. Zhang, M. Li, X. Gao, X. Li, Multifunctional polymer-regulated SnO₂ nanocrystals enhance interface contact for efficient and stable planar perovskite solar cells, *Adv. Mater.* 32 (2020) 2003990, <https://doi.org/10.1002/adma.202003990>.
- [33] H.-J. Kim, M.-H. Piao, S.-H. Choi, C.-H. Shin, Y.-T. Lee, Development of Amperometric Hydrogen Peroxide Sensor Based on Horseradish Peroxidase-Immobilized Poly(Thiophene-co-EpoxyThiophene), *Sensors* 8 (2008) 4110–4118, <https://doi.org/10.3390/s8074110>.
- [34] J. Kim, M. Kim, H. Kim, J. Yang, TiO₂ thin film deposition by RF reactive sputtering for nip planar structured perovskite solar cells, *Appl. Sci. Conver. Technol.* 31 (2022) 116–119, <https://doi.org/10.5757/ASCT.2022.31.5.116>.
- [35] N. Lalpour, V. Mirkhani, R. Keshavarzi, M. Moghadam, S. Tangestaninejad, I. Mohammadpoor-Baltork, P. Gao, Self-healing perovskite solar cells based on copolymer-templated TiO₂ electron transport layer, *Sci. Rep.* 13 (2023) 6368, <https://doi.org/10.1038/s41598-023-33473-9>.
- [36] J. Kruszyńska, J. Ostapko, V. Ozkaya, B. Surucu, O. Szawcow, K. Nikiforow, M. Holdynski, M.M. Tavakoli, P. Yadav, M. Kot, Atomic layer engineering of aluminum-doped zinc oxide films for efficient and stable perovskite solar cells, *Adv. Mater. Interfaces* 9 (2022) 2200575, <https://doi.org/10.1002/admi.202200575>.
- [37] J.J. Yoo, S. Wiegold, M.C. Sponseller, M.R. Chua, S.N. Bertram, N.T.P. Hartono, J. S. Tresback, E.C. Hansen, J.-P. Correa-Baena, V. Bulović, An interface stabilized perovskite solar cell with high stabilized efficiency and low voltage loss, *Energy Environ. Sci.* 12 (2019) 2192–2199, <https://doi.org/10.1039/C9EE00751B>.
- [38] H. Min, D.Y. Lee, J. Kim, G. Kim, K.S. Lee, J. Kim, M.J. Paik, Y.K. Kim, K.S. Kim, M. G. Kim, T.J. Shin, S. Il Seok, Perovskite solar cells with atomically coherent interlayers on SnO₂ electrodes, *Nature* 598 (2021) 444–450, <https://doi.org/10.1038/s41586-021-03964-8>.
- [39] W. Zhu, Z. Zhang, W. Chai, Q. Zhang, D. Chen, Z. Lin, J. Chang, J. Zhang, C. Zhang, Y. Hao, Band alignment engineering towards high efficiency carbon-based inorganic planar CsPbI₃ perovskite solar cells, *ChemSusChem* 12 (2019) 2318–2325, <https://doi.org/10.1002/cssc.201900611>.
- [40] T. Imran, S. Rauf, H. Raza, L. Aziz, R. Chen, S. Liu, J. Wang, M.A. Ahmad, S. Zhang, Y. Zhang, Z. Liu, W. Chen, Methylammonium and bromide-free tin-based low bandgap perovskite solar cells, *Adv. Energy Mater.* 12 (2022) 2200305, <https://doi.org/10.1002/aenm.202200305>.
- [41] D. Madadi, I. Gharibshahian, A.A. Orouji, High-performance α-FAPbI₃ perovskite solar cells with an optimized interface energy band alignment by a Zn(O,S) electron transport layer, *J. Mater. Sci.: Mater. Electron.* 34 (2023) 51, <https://doi.org/10.1007/s10854-022-09565-z>.
- [42] Z. Jiang, D. Wang, J. Sun, B. Hu, L. Zhang, X. Zhou, J. Wu, H. Hu, J. Zhang, W.C. H. Choy, B. Xu, Quenching detrimental reactions and boosting hole extraction via multifunctional NiO_x/perovskite interface passivation for efficient and stable inverted solar cells, *Small Methods* 8 (2024) 2300241, <https://doi.org/10.1002/smt.202300241>.
- [43] X. Ji, L. Bi, Q. Fu, B. Li, J. Wang, S.Y. Jeong, K. Feng, S. Ma, Q. Liao, F. Lin, Target therapy for buried interface enables stable perovskite solar cells with 25.05% efficiency, *Adv. Mater.* (2023) 2303665, <https://doi.org/10.1002/adma.202303665>.
- [44] R. Guo, D. Han, W. Chen, L. Dai, K. Ji, Q. Xiong, S. Li, L.K. Reb, M.A. Scheel, S. Pratap, N. Li, S. Yin, T. Xiao, S. Liang, A.L. Oechsle, C.L. Weindl, M. Schwartzkopf, H. Ebert, P. Gao, K. Wang, M. Yuan, N.C. Greenham, S. D. Stranks, S.V. Roth, R.H. Friend, P. Müller-Buschbaum, Degradation mechanisms of perovskite solar cells under vacuum and one atmosphere of nitrogen, *Nat. Energy* 6 (2021) 977–986, <https://doi.org/10.1038/s41560-021-0912-8>.
- [45] L. Xie, J. Liu, J. Li, C. Liu, Z. Pu, P. Xu, Y. Wang, Y. Meng, M. Yang, Z.J.A.M. Ge, A deformable additive on defects passivation and phase segregation inhibition enables the efficiency of inverted perovskite solar cells over 24%, *Adv. Mater.* (2023) 2302752, <https://doi.org/10.1002/adma.202302752>.
- [46] W. Kim, M.S. Jung, S. Lee, Y.J. Choi, J.K. Kim, S.U. Chai, W. Kim, D.G. Choi, H. Ahn, J.H. Cho, Oriented grains with preferred low-angle grain boundaries in halide perovskite films by pressure-induced crystallization, *Adv. Energy Mater.* 8 (2018) 1702369, <https://doi.org/10.1002/aenm.201702369>.
- [47] D. Di Girolamo, N. Phung, F.U. Kosasih, F. Di Giacomo, F. Matteocci, J.A. Smith, M. A. Flatken, H. Köbler, S.H. Turren Cruz, A. Mattoni, Ion migration-induced amorphization and phase segregation as a degradation mechanism in planar perovskite solar cells, *Adv. Energy Mater.* 10 (2020) 2000310, <https://doi.org/10.1002/aenm.202000310>.
- [48] A. Alberti, C. Bongiorno, E. Smecca, I. Deretzi, A. La Magna, C. Spinella, Pb clustering and PbI₂ nanofragmentation during methylammonium lead iodide perovskite degradation, *Nat. Commun.* 10 (2019) 2196, <https://doi.org/10.1038/s41467-019-09909-0>.
- [49] E. Aydin, M. De Bastiani, S. De Wolf, Defect and contact passivation for perovskite solar cells, *Adv. Mater.* 31 (2019) 1900428, <https://doi.org/10.1002/adma.201900428>.
- [50] J. Wu, J. Shi, Y. Li, H. Li, H. Wu, Y. Luo, D. Li, Q. Meng, Quantifying the interface defect for the stability origin of perovskite solar cells, *Adv. Energy Mater.* 9 (2019) 1901352, <https://doi.org/10.1002/aenm.201901352>.
- [51] G. Benecke, W. Wagermaier, C. Li, M. Schwartzkopf, G. Flucke, R. Hoerth, I. Zizak, M. Burghammer, E. Metwalli, P. Müller-Buschbaum, M. Trebbin, S. Forster, O. Paris, S.V. Roth, P. Fratzl, A customizable software for fast reduction and analysis of large X-ray scattering data sets: applications of the new DPDAK package to small-angle X-ray scattering and grazing-incidence small-angle X-ray scattering,

J. Appl. Crystallogr. 47 (2014) 1797–1803, <https://doi.org/10.1107/S1600576714019773>.

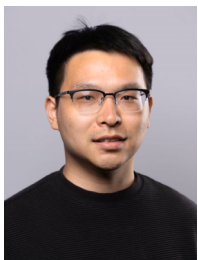
- [52] W. Cao, J. Zhang, K. Lin, L. Qiu, J. Li, Y. Dong, D. Xia, Y. Yang, Redox engineering of spiro-OMeTAD based hole transport layer enabled by ultrathin Co(III)-grafted carbon nitride nanosheets for stable perovskite solar cells, *Nano Energy* 104 (2022) 107924, <https://doi.org/10.1016/j.nanoen.2022.107924>.
- [53] M.A. Reus, L.K. Reb, D.P. Kosbahn, S.V. Roth, P. Müller-Buschbaum, INSIGHT: in situ heuristic tool for the efficient reduction of grazing-incidence X-ray scattering data, *J. Appl. Crystallogr.* 57 (2024), <https://doi.org/10.1107/S1600576723011159>.



Xiongzhao Jiang received his master's degree in material science from the South China University of Technology in 2021. He is currently a Ph.D. student at the School of Natural Sciences, Technical University of Munich, under the supervision of Professor Peter Müller-Buschbaum since 2022. His research focuses on the growth of perovskite films and the degradation mechanisms of perovskite solar cells using synchrotron-based X-ray scattering techniques.



Jie Zeng received his M.E degree from the Materials Engineering, Southern University of Science and Technology (SUSTech), in June 2021. He is currently a Ph.D. candidate at the Department of Materials Science and Engineering of City University of Hong Kong. His research interests include large-area perovskite solar cells, device encapsulation, and module recycling.



Kun Sun is currently a Ph.D. student at the School of Natural Sciences, Technical University of Munich, under the supervision of Professor Peter Müller-Buschbaum. His research focuses on the growth of perovskite films and the degradation mechanisms of perovskite solar cells using synchrotron-based X-ray scattering techniques.



Zerui Li received his B.S. degree in Material Chemistry and M. S. degree in Chemical Engineering from University of Science and Technology of China (USTC). He is now completing the Ph. D. degree in Physics at Technical University of Munich (TUM) since 2021. He is a member of the Chair for Functional Materials (E13) at TUM, which focuses on the microstructure of thin films with advanced X-ray scattering techniques. His current research mainly focuses on the degradation mechanism and stability improvement strategies for organic solar cells, as well as film formation process analysis and high efficiency device fabrication.



Zhuijun Xu received his master's degree in Ningbo Institute of Materials Technology & Engineering, Chinese Academy of Sciences, Ningbo, P. R. China, and joined Technical University of Munich, TUM School of Natural Sciences, Department of Physics, E13 in 2021. His research focuses on the fields of energy storage materials, in-situ X-ray technology (in situ GISAXS, in-situ GiWAXS, in-situ XRD), and sputtering.



Guangjiu Pan received his bachelor's degree from Jiangxi University of Science and Technology (2017) and his master's degree from Central South University (2020). Currently, he is a PhD candidate in Physics at Technical University of Munich, under the supervision of Prof. Dr. Peter Müller-Buschbaum since 2021. His research interests include the synthesis of mesoporous metal oxides based on block copolymer self-assembly and advanced X-ray scattering techniques.



Dr. Renjun Guo is currently a Research Group Leader at the Institute for Microstructure Technology, Karlsruhe Institute of Technology (KIT), Germany, focusing on high-efficiency perovskite solar cells and synchrotron radiation-based materials characterization techniques. With extensive international research experience, he previously worked as a postdoctoral researcher at the National University of Singapore and the Solar Energy Research Institute of Singapore, where he contributed to cutting-edge projects and achieved several breakthrough results. He has published numerous high-impact papers in top international journals. His leadership in research projects spans the development of perovskite tandem cells and new energy materials with significant academic and industrial applications.



Dr. Suzhe Liang currently is a postdoctoral researcher at Eastern Institute for Advanced Study, Eastern Institute of Technology, Ningbo, China. He earned his Dr. rer. nat degree at Technical University of Munich (TUM), Germany in 2024. His research interests involve all-solid-state battery interfaces, anode materials for lithium/sodium-ion batteries, and in situ X-ray scattering techniques.



Yusuf Bulut is a Ph.D. student at Deutsches Elektronen-Synchrotron (DESY) in the Sustainable Materials group FS-SMA headed by Prof. Roth since 2021 and with main supervisor Prof. Müller-Buschbaum at the Chair of Functional Materials at the Technical University of Munich. His research focuses on the in-situ investigation of thin films produced under standard and reactive sputtering conditions on polymer surfaces using grazing incidence small-angle X-ray scattering (GISAXS) and grazing incidence small- and wide-angle X-ray scattering (GIWAXS).



Dr. **Benedikt Sochor** is an experimental physicist who received his PhD from the University of Würzburg (Germany) in 2021. Since then, he has worked on surface and interface characterization at the synchrotron beamline P03 of PETRA III (DESY, Hamburg, Germany). He is also affiliated with the Advanced Light Source (Lawrence Berkeley National Laboratory, Berkeley, California).



Prof. Dr. **Franz Faupel** received his Ph.D. in physics from the University of Göttingen in 1985. He was postdoctoral fellow at the IBM Research Center Yorktown Heights and received his habilitation in 1992. Since 1994, he holds the Chair for Multicomponent Materials at Kiel University. He is Chairman of the North European Initiative Nanotechnology and a founding member of the newly established International Alliance of Societies for a Sustainable Future. He has served on various editorial boards including the Journal of Materials Research, SN Applied Sciences, Materials, Applied Physics Letters, and Journal of Applied Physics. He published over 400 research papers.



Dr. **Matthias Schwartzkopf** received his Diploma degree in Chemistry from Technical University in Berlin and his PhD at University of Hamburg. He is presently a committed staff scientist at the P03 beamline of PETRA III light source, Photon Science, DESY in Hamburg with outstanding experience of conducting X-ray related soft matter research in collaboration with an international interdisciplinary user community. His research interests are focused on combined real-time surface-sensitive X-ray scattering at functional nanomaterials for advancing information and energy technologies.



Prof. Dr. **Stephan V. Roth** is heading the Sustainable Materials group at Deutsches Elektronen-Synchrotron (DESY), Hamburg, Germany, focusing on functionalized bio-based polymer materials, and is professor for scattering-based characterization techniques in fibre and polymer technology at KTH Royal Institute of Technology in Stockholm, Sweden. His research in sustainability includes the development of hybrid materials from renewable resources for flexible electronics and photovoltaics, the development of green processes in thin film technology using the principles of green chemistry and the application of machine learning for advanced data analysis.



Kristian A. Reck received his master's degree in physics from the University of Kiel, Germany, with a focus on plasma physics and diagnostics. He is currently a PhD student at the Chair of Multicomponent Materials at the Department of Materials Science at Kiel University. His research focuses on the effects of HiPIMS on the early growth stages during the deposition of metals and oxides on polymers, which are analyzed using in-situ GISAXS and GIWAXS, among others.



Dr. **Baomin Xu** is a Chair Professor at the Department of Materials Science and Engineering, Southern University of Science and Technology (SUSTech), Shenzhen, China. He received the B.Eng. degree from Tsinghua University in 1986, and Ph.D. degree from Shanghai Institute of Ceramics, Chinese Academy of Sciences in 1991. Prof. Xu's current research interests are focused on clean energy materials and devices, and their novel fabrication technologies, including solar cells, rechargeable batteries, and supercapacitors. He is an inventor of 32 granted US patents and author or co-author of more than 220 publications.



Dr. **Thomas Strunskus** is a senior researcher at the Chair for Multicomponent Materials (Prof. Franz Faupel). He received his Ph.D. from the University of Heidelberg investigating metal-polymer interfaces. In 1994 he joined Prof. Faupel at CAU Kiel as one of his assistants. His focus was on vapor-phase deposition and analysis of metal-polymer nanocomposites. From 2001–2006 he moved to the physical chemistry group of Prof. Wöll at Bochum University, leading the surface analysis and synchrotron radiation activities. In 2006 he moved back to the group of Prof. Faupel leading again the nanocomposite activities while staying active in synchrotron radiation based research.



Prof. Dr. **Peter Müller-Buschbaum** is full professor at Technical University of Munich, heading the Chair for Functional Materials since 2006. Presently, he is heading the keylab 'TUM. solar' on solar energy conversion and storage and the 'Network for Renewable Energies' of the 'Munich Institute of Integrated Materials, Energy and Process Engineering (MEP)'. He is the German representative at the 'European Polymer Federation' (EPF) for polymer physics. He is elected chairman of the 'Hamburg User Committee' (HUC) at the synchrotron radiation laboratory DESY, a member of the 'European Synchrotron User Organization' (EUSO) and deputy editor of ACS Applied Materials & Interfaces.